Defect-engineered room-temperature ferromagnetism in quasi-two-dimensional nitrided $CoTa_2O_6$

Yalin Ma,[1] Shuang Zhao,[1] Xiao Zhou,[1] Yijie Zeng,[2,3,*] Haili Song,[1] Jing Wang,[1] Guangqin Li,[1] Corey E. Frank,[4] Lu Ma,[5] Mark Croft,[6] Yonggang Wang,[7] Martha Greenblatt,[4] Dao-Xin Yao,[2,†] and Man-Rong Li[1,‡]

[1]*Key Laboratory of Bioinorganic and Synthetic Chemistry of Ministry of Education, School of Chemistry, Sun Yat-Sen University, Guangzhou 510275, China*

[2]*State Key Laboratory of Optoelectronic Materials and Technologies, School of Physics, Sun Yat-Sen University, Guangzhou 510275, China*

[3]*College of Science, Hangzhou Dianzi University, Hangzhou 310018, China*

[4]*Department of Chemistry and Chemical Biology, Rutgers, The State University of New Jersey, 123 Bevier Road, Piscataway, New Jersey 08854, USA*

[5]*Brookhaven National Laboratory, National Synchrotron Light Source II, Building 74, P.O. Box 5000, Upton, New York 11973-5000, USA*

[6]*Department of Physics and Astronomy, Rutgers, The State University of New Jersey, 136 Frelinghuysen Road, Piscataway, New Jersey 08854, USA*

[7]*Center for High Pressure Science and Technology Advanced Research (HPSTAR), Beijing 100094, China*

(Received 5 April 2021; accepted 1 July 2021; published 19 July 2021)

Thermal ammonolysis of quasi-two-dimensional (quasi-2D) $CoTa_2O_6$ yields the O^{2-}/N^{3-} and anionic vacancy-ordered $Co^{2+}Ta_2^{5+}O_{6-x}N_{2x/3}\square_{x/3}$ ($x \leqslant 0.15$), which exhibits a transition from antiferromagnetism to defect-engineered above-room-temperature ferromagnetism. First-principles calculations reveal that the origin of ferromagnetism is a particular CoO_5N configuration with N located at Wyckoff position 8*j*, which breaks mirror symmetry about the *ab* plane. A pressure-induced electronic phase transition is also predicted at $\sim$ 24.5 GPa, accompanied by insulator-to-metal transition and magnetic moment vanishing.

DOI: 10.1103/PhysRevB.104.014421

I. INTRODUCTION

Room-temperature (RT) ferromagnetic (FM) insulators have opened a fascinating field of multiferroics and spintronic devices [1–5]. Recently, diluted magnetic semiconductors (DMSs) played a major role in this field. Magnetic ions doped nonmagnetic oxides, such as Co-doped TiO_2, Cr, Mn, Ni, or Nd-doped ZnO [3,6–9], can induce long-range FM order deriving from the strong electron exchange interactions of the guest dopant. Later on, it was found that vacancy-driven defect engineering, such as the incorporation of oxygen or transition metal vacancies, can also facilitate RT FM interactions in nonmagnetic oxides such as CaO, MgO, ZnO, TiO_2, Al_2O_3, and others [10–14]. Furthermore, hydrostatic pressure offers systematic control for tuning electrical and magnetic properties, as reported in two-dimensional (2D) van der Waals (vdW) materials. The magnetic response of 2D chalcogenides can be tuned by external pressure, as discovered in the confined two-layered CrI_3, which revealed a pressure-induced antiferromagnetic (AFM)-to-FM transition at 2.7 GPa, providing thermodynamic freedom for optimized performance [15–17]. Multilayered MoS_2 and WS_2 undergo a semiconductor-to-metal transition at $\sim$19 and 22 GPa, respectively [18,19], originating from sulfur-sulfur interactions as the interlayer spacing reduces with the increment of pressure.

These findings point out an effective approach to search for RT FM insulators, semiconductors, or metals in 2D materials by dimensional controlling, defect engineering, and/or compressing. In contrast to the flourishing success in low-dimensional chalcogenides [4,20–23], there are relatively few studies devoted to FM insulator design in the chemically benign (stable and easy synthesis) 2D oxides [24]. In this paper, we ammoniated the trirutile-type $CoTa_2O_6$ (CTO), and successfully realized the transition from initial antiferromagnetism to above-RT ferromagnetism via anionic defect engineering in the nitridated product. The crystal and electronic structures of as-made samples were extensively studied by diffraction and spectroscopic techniques. Defect-dependent magnetism evolution was also experimentally and theoretically studied. First-principles calculations were conducted to reveal the origin of the above-RT magnetism, estimate the band gap, and evaluate the evolution of magnetism and conductivity under high pressure.

II. RESULTS AND DISCUSSION

A. Phase and structural characterizations

Figure 1(a) (bottom) shows powder x-ray diffraction (XRD) patterns of CTO, which is consistent with the reported tetragonal $P4_2/mnm$ cell [25]. The precursor was treated under NH_3 flow at temperatures ranging from 650 to 900 °C. Attempts to azotize CTO <650 °C or >800 °C were unsuccessful since the precursor remained either unchanged (<650 °C) or started to decompose (>800 °C). Figure 1(a)

*zengyj@hdu.edu.cn
†yaodaox@mail.sysu.edu.cn
‡limanrong@mail.sysu.edu.cn

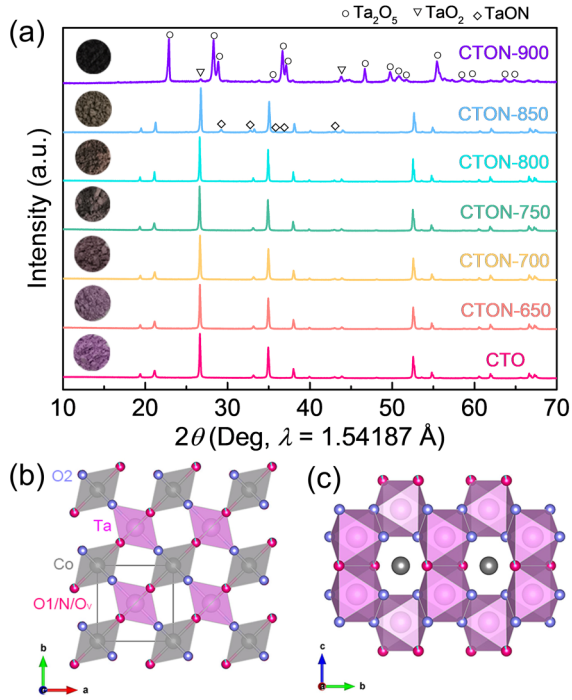

FIG. 1. (a) X-ray diffraction (XRD) patterns of $CoTa_2O_{6-x}N_{2x/3}\square_{x/3}$ prepared at various temperatures under NH_3 flow. The XRD patterns of CTO precursor are on the bottom for comparison. Left insert shows the color evolution of $CoTa_2O_{6-x}N_{2x/3}\square_{x/3}$ powder. Crystal structure of $CoTa_2O_{6-x}N_{2x/3}\square_{x/3}$, with the view of (b) layered structure along the *c* axis and (c) honeycomblike ring along the *a* axis. The light silver octahedra are $CoO_{6-x}N_{2x/3}$, the light pink octahedra are $TaO_{6-x}N_{2x/3}$, Co is represented by silvery gray, Ta light pink, O1 rosy red, N/□ (oxygen vacancies) cyan, O2 violet. The N atoms and oxygen vacancies are distributed at the O1 site.

displays the XRD patterns of CTO after azotized at different temperatures. The as-nitrided $CoTa_2O_{6-x}N_{2x/3}$ samples are hereafter denoted as CTON-650, CTON-700, CTON-750, CTON-800, CTON-850, and CTON-900, respectively, according to the reaction temperature. The normalized XRD patterns of CTO and CTON-800 are compared in Fig. S1 (Supplemental Material [26]), which indicates slightly weakened intensity of most XRD peaks in CTON-800 except the one at 21.1 °. In addition, the color of $CoTa_2O_{6-x}N_{2x/3}$ successively gets darker with temperature increment [Fig. 1(a)], starting from pink for CTO, passing through dark pink (CTON-650 and CTON-700) to gray (CTON-750 and CTON-800). This variation of optical absorption indicates the enhanced N^{3-} incorporation into CTO at elevated temperatures [27,28], as further corroborated by thermogravimetric analysis (TGA) in air (Fig. S2, Supplemental Material [26]) discussed below.

The N incorporation in $CoTa_2O_{6-x}N_{2x/3}$ was evaluated by TGA as depicted in Fig. S2 (Supplemental Material [26]). The weight variation <200 °C in Figs. S2(a)–S2(c) (Supplemental Material [26]) is attributed to physical absorption. All oxynitrides undergo a stage of mass gain <∼700 °C, owing to the release of nitrogen and reoxidation process (Figs. S2(b)–S2(d), Supplemental Material [26]) [29]. The TGA curves exhibit further weight loss after the oxidation process >700 °C, probably due to the decomposition of intermediate compounds [30]. The nitrogen-richest compound CTON-800 is more reactive, as evidenced by the onset of oxidation-induced weight gaining started >320 °C, in comparison with that from 560 and 446 °C for CTON-700 and CTON-750, respectively. Accordingly, the *x* value in $CoTa_2O_{6-x}N_{2x/3}$ can be estimated from these data, as each weight increment is equal to the difference between released N_2 and uptake O_2 [31,32]. Figure S3 (Supplemental Material [26]) shows XRD patterns for $CoTa_2O_{6-x}N_{2x/3}$ samples after TGA measurements [26], indicating that the nitrided samples reverted to CTO. There is no evidence of Co^{3+} formation during the oxygenating process. The TGA weight gains were determined to be 0.0174(3)%, 0.0627(12)%, and 0.1859(7)% corresponding to CTON-700, CTON-750, and CTON-800 with $x = 0.015(1)$, 0.05(1), and 0.15(1), respectively. To maintain charge balance in $CoTa_2O_{6-x}N_{2x/3}$, the substitution of O^{2-} by N^{3-} simultaneously generates anion vacancies since Co^{3+} is unlikely to survive in the reducing NH_3 atmosphere, giving nominal formula of $CoTa_2O_{6-x}N_{2x/3}\square_{x/3}$ (where □ denotes the anionic vacancy). Transmission electron microscopy and energy-dispersive x-ray spectroscopy (TEM-EDS) analysis confirms the Co/Ta ratio [∼1/1.92(6)] of CTON-800 and homogeneous Co and Ta distribution (Fig. S4, Supplemental Material [26]). As N content increased, the band gap (E_g) exhibited a narrowing from the initial 3.22 to 3.02 eV, which is estimated by ultraviolet (UV)-visible diffuse reflectance spectra (UV-Vis DRS, Fig. S5, Supplemental Material [26]) [25,33,34].

Figure S6(a) (Supplemental Material [26]) shows the refined plots of XRD patterns for CTO in the reported $P4_2/mnm$ space group (No. 136, $a = 4.7375\,(4)$ Å, $c = 9.1764\,(9)$ Å, $V = 205.95\,(5)$ Å^3, and $Z = 2$) [35–37]. $CoTa_2O_{6-x}N_{2x/3}\square_{x/3}$ ($x = 0.015$, 0.05, and 0.15) are isostructural to CTO, and the same starting model was applied for their structure refinements as exhibited in Figs. S6(b)–S6(d) (Supplemental Material [26]). The refined crystallographic parameters and selected interatomic distances and angles are summarized in Tables S1 and S2 (Supplemental Material [26]). Although the effective ionic radius of N^{3-} ion ($r_{\text{eff}} = 1.46$ Å) is slightly larger than that of O^{2-} ($r_{\text{eff}} = 1.38$ Å) [38], the lattice parameter tends to be constant in different N content, resulting from the associated increase of anionic vacancies, as shown in Fig. S7 (Supplemental Material [26]). Previous studies show that high-valency metal cations with smaller ionic radius can sometimes form to keep charge balance in a number of perovskite oxynitrides [39–41]. However, the ammonolysis process drives the more electronegative 3*d* transition metals Fe, Co, Ni, and Cu to form interstitial nitrides with low positive oxidation states [40]. It is thus unlikely to form Co^{3+} by ammonolysis of $Co^{2+}Ta_2^{5+}O_6$. The formal oxidation state of cations in $CoTa_2O_{6-x}N_{2x/3}\square_{x/3}$ is further supported by x-ray absorption near edge spectroscopy (XANES, Fig. S8, Supplemental Material [26]) and x-ray photoelectron spectroscopy (XPS, Fig. S9, Supplemental Material [26]) measurements [37,42–59]. Fourier transform infrared (FT-IR) spectroscopy results also confirm the interactions among chemical bonds in $CoTa_2O_{6-x}N_{2x/3}\square_{x/3}$ (Fig. S10, Supplemental Material [26]) [60–64]. In addition, the 2D

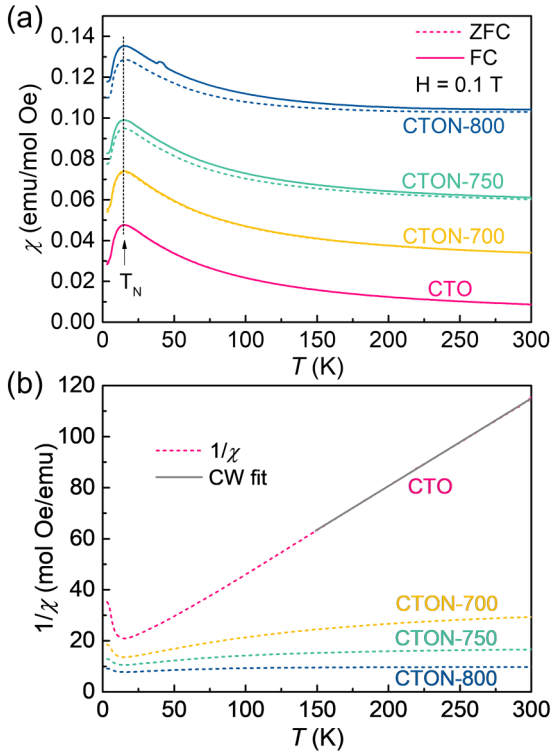

FIG. 2. Magnetic properties of $CoTa_2O_{6-x}N_x\square_{x/3}$. (a) Temperature dependence of zero-field-cooled (ZFC; short dash line) and field-cooled (FC; solid line) χ curves of CTO, CTON-700, CTON-750, and CTON-800, measured at 0.1 T. (b) The ZFC χ^{-1} vs T curves of CTO, CTON-700, CTON-750, and CTON-800, measured at 0.1 T. The solid line shows the Curie-Weiss (CW) fitting of the paramagnetic region between 150 and 300 K.

honeycomb-layered $CoTa_2O_{6-x}N_{2x/3}\square_{x/3}$ compounds have the same six-coordinated Co and Ta ions [Figs. 1(b) and 1(c)] as in CTO. The O1/N anions and vacancies were distributed at the $4f$ $(x, y, 0)$ sites, while O2 ions fully occupy $8j$ (x, y, z) sites during refinements according to the calculated results (vide infra).

B. Magnetic properties

Figure 2(a) shows the temperature-dependent magnetic susceptibility $\chi(T)$ of $CoTa_2O_{6-x}N_{2x/3}\square_{x/3}$ ($x = 0.015$, 0.05, and 0.15) with $T = 5$–300 K measured at $H = 0.1$ T in zero-field-cooled (ZFC) and field-cooled (FC) modes. It is clearly seen that bulge peaks of all samples arise in the ZFC and FC curves [Fig. 2(a)], illustrating the predominance of AFM phase transition at $T_N = 14.7$ K, which is close to the literature result [65]. Notably, unlike CTO, the ZFC and FC curves of N-containing samples do not overlap until up to 300 K [Fig. 2(a)] in analogous-to-ZnO nanosheets [66], indicating the existence of RT ferromagnetism. Above 150 K, the ZFC $1/\chi - T$ curve for CTO can be fitted with the Curie-Weiss (CW) law, $1/\chi = (T - \theta_W)/C$, where $C = \mu_{eff}^2/8$ is the Curie constant, θ_W is Weiss temperature, and μ_{eff} is the effective magnetic moment [Fig. 2(b)]. The $\theta_W = -35$ K is consistent with AFM order. The value of μ_{eff} for CTO was calculated to be 4.82 μ_B, which agrees well to the typical value for high-spin Co^{2+} ($S = \frac{3}{2}$) in octahedral geometry. In Fig. 2(b), in contrast to CTO, the $1/\chi - T$ curves for CTON-700, CTON-750, and CTON-800 exhibit nearly temperature-independent behavior at $T > 50$ K and do not obey the CW law, implying different magnetic interaction mechanism in anionic vacancy-rich cases.

Additional characterization of the nature of magnetic transition in $CoTa_2O_{6-x}N_{2x/3}\square_{x/3}$ samples was achieved through isothermal field-dependent magnetization $M(H)$ measured between 5 and 550 K, and applied magnetic field from −4 to 4 T (Figs. 3 and S11, Supplemental Material [26]). As shown in Fig. 3(a), the magnetization curves for CTO show no hysteresis at 10 and 250 K, supported the AFM interactions. Interestingly, CTON-700, CTON-750, and CTON-800 samples show slight hysteretic loops over the experimental temperature range, indicating a RT FM feature [Figs. 3(b)–3(d)]. Their saturation magnetizations slightly decrease with increasing temperature, which is attributed to the changes in the magnetic moment of cobalt beside anion vacancies. Note that the nitrided series have larger slope values (M/H) in $0 < H < 0.5$ T than those in $H > 0.5$ T. We assume that the AFM coupling is weakened with enhanced nitrogen incorporation, and it might be accompanied by the appearance of weak FM states in $0 < H < 0.5$ T, as displayed in Fig. S12 (Supplemental Material [26]). For DMS materials, the formation of oxygen vacancies lowers the valence of the metal ions and thus entangles ferromagnetism, while the vdW materials such as CrI_3 and VSe_2 conceive intrinsic ferromagnetism in exfoliated monolayer [4,67]. As for $CoTa_2O_{6-x}N_{2x/3}\square_{x/3}$, neither valence transition nor thickness-dependent layer interface exists; the emergent RT ferromagnetism differs from known studies. Therefore, theoretical calculations were performed to figure out the origin of emerging ferromagnetism.

C. Theoretical calculations

1. Bulk electronic structure: k-dependent spin splitting

Although the magnetic structure of CTO is controversial and not fully determined [68], it was corroborated that the magnetic moments of Co atoms lie in the ab plane and antiferromagnetically coupled along [110] on $z = 0$ and [−110] on $z = c/2$, with propagation vectors $(\pm\frac{1}{4}, \frac{1}{4}, \frac{1}{4})$. To model such a magnetic structure accurately would require a supercell containing 576 atoms, which is beyond the capability of the modern first-principles calculation method [69–72]. Thus, in our calculations, only spin-polarization calculation is adopted, and some meaningful results are obtained.

The band structure of AFM CTO shows k-dependent spin splitting [73], which is different from those of conventional antiferromagnets whose spin-up and spin-down energy levels are degenerate along all k-points in the Brillouin zone (BZ). Here, the spin-up and spin-down energy levels of CTO are nondegenerate along ΓM $(u, u, 0)$ and ZA $(v, v, 0.5)$ (where $0 < u, v < 0.5$), both of which are along the (110) direction of the BZ. This spin splitting energy is as large as 150 meV for the valence band below the Fermi energy, much larger than the splitting caused by spin-orbit coupling for $3d$ transition metals [74]. This behavior can be understood as follows [75]. In AFM spin-polarized calculations, the magnetic moments of Co atoms are directed along the z direction, which reduces the Shubnikov group of CTO from paramagnetic $P4_2/mnm1'$

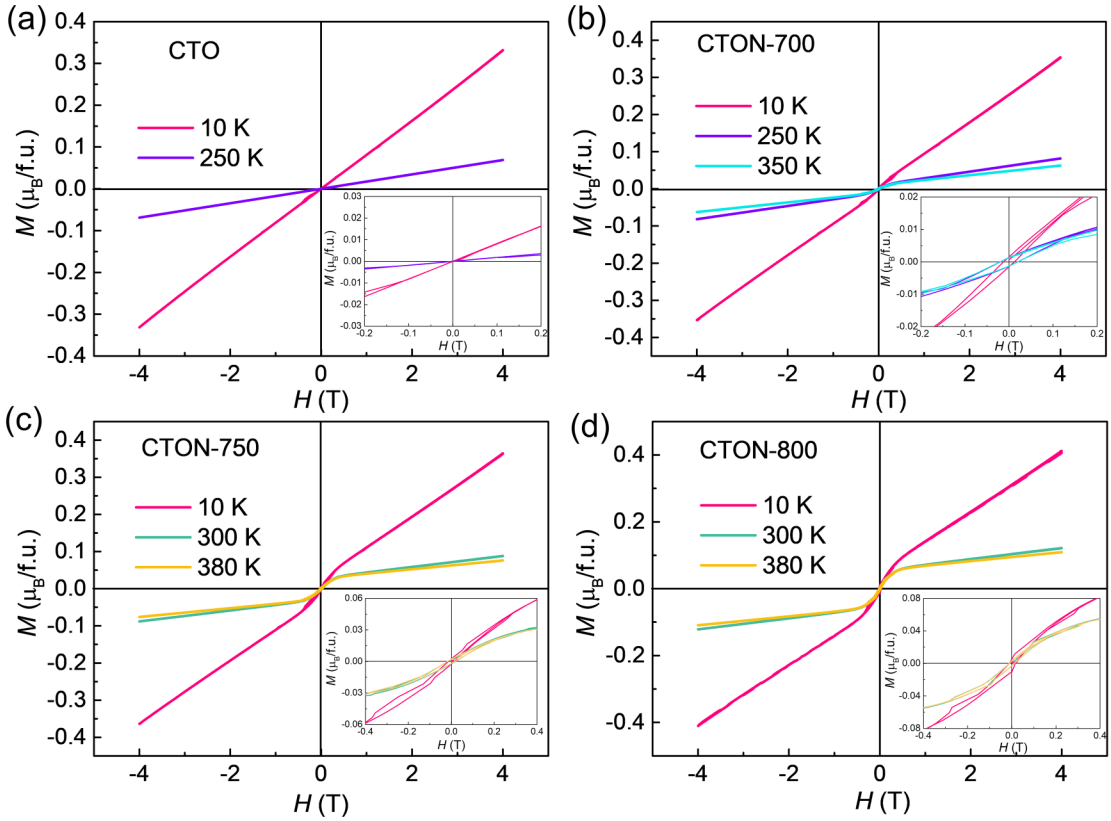

FIG. 3. Isothermal magnetization curves of $CoTa_2O_{6-x}N_x\square_{x/3}$ at 10, 250, 300, 350, and 380 K between −4 and 4 T. (a) CTO, (b) CTON-700, (c) CTON-750, and (d) CTON-800. The insets in (a) and (b) show the enlarged area between −0.2 and 0.2 T, in (c) and (d) between −0.4 and 0.4 T.

(BNS [76]: 136.496) to AFM $P4'_2/mnm'$ (BNS: 136.499). In the former case, time-reversal symmetry ensures double degeneracy for all energy levels at all k-points, namely, spin-up and spin-down energy levels are degenerate. In the latter case, however, time-reversal symmetry is broken, but its combination of some space group symmetry operations exists. The group of wave vectors at Σ $(\alpha, \alpha, 0)$ $(0 < \alpha < \pi/a)$, for example, is {(1|0, 0, 0), (2 − xy|0, 0, 0),' (mz| 0, 0, 0), (mxy|0, 0, 0)' }$a = C_{2v}$ (C_s), of which the single-valued representations (Σ_1, Σ_2) are both one dimensional [75]. Thus, the energy levels at Σ are nondegenerate, as revealed by the spin-splitting of the energy bands along ΓM. Similar explanations can be applied to other k vectors, and the detailed labeling of the representations are shown in Fig. 4(a).

Figure 4(b) provides the calculated magnetization density around the two Co atoms. The magnetization is defined as $m(r) = \rho^{\uparrow}(r) - \rho^{\downarrow}(r)$, where $\rho^{\uparrow}(r)$ and $\rho^{\downarrow}(r)$ are spin-up and spin-down electron densities, respectively. The magnetization shows clear anisotropy in the ab plane, indicating the magnetic moments of Co atoms at the corner tend to align toward [110] or [−1-10] and those at the center toward [1–3,3–9] or [−110], but the absolute direction cannot be determined.

The k-dependent spin-splitting causes the density of states (DOS) to be asymmetric for spin-up and spin-down channels, as shown in Fig. 5. Here, both the PBE and LDA + U results are shown. The PBE result underestimates the band gap to ∼0.5 eV, which is a well-known problem of density functional theory. The LDA + U method remedies this problem effectively and gives a band gap ∼2.7 eV, which is close to the experimental value, too insulating to be measured within the ammeter range [77]. However, the crystal field splitting of the Co d orbitals, caused by the oxygen octahedron, appears clearly near the Fermi energy in the PBE-derived DOS, but is lost in the LDA + U one due to the large onsite Coulomb interaction since the magnetic susceptibility and crystal field splitting are ground state properties, while band gap is related with excitation states. Moreover, density functional theory [78,79] is expected to work well only for ground state property. We propose to rely on the PBE results to discuss the magnetic property.

2. The effect of nitrogen dopant on the electronic structure: from antiferromagnet to ferrimagnet

The $x = 0.3$ case of $CoTa_2O_{6-x}N_{2x/3}\square_{x/3}$ other than the experimental $x = 0.15$ is considered in our calculations to avoid too large of a supercell, with the crystal structure shown in Figs. 6(a) and 6(b). This increase of dopant ratio should not cause trouble because the distance between vacancies is already small in the $x = 0.3$ case. Since there are two types of oxygen atoms in the bulk crystal of CTO, with location at Wyckoff position 4f or 8j, the oxygen vacancy is thus put to either 4f or 8j. One nitrogen atom is near the oxygen vacancy, at the same Wyckoff position, and the other nitrogen is away from the oxygen vacancy, at the opposite Wyckoff position.

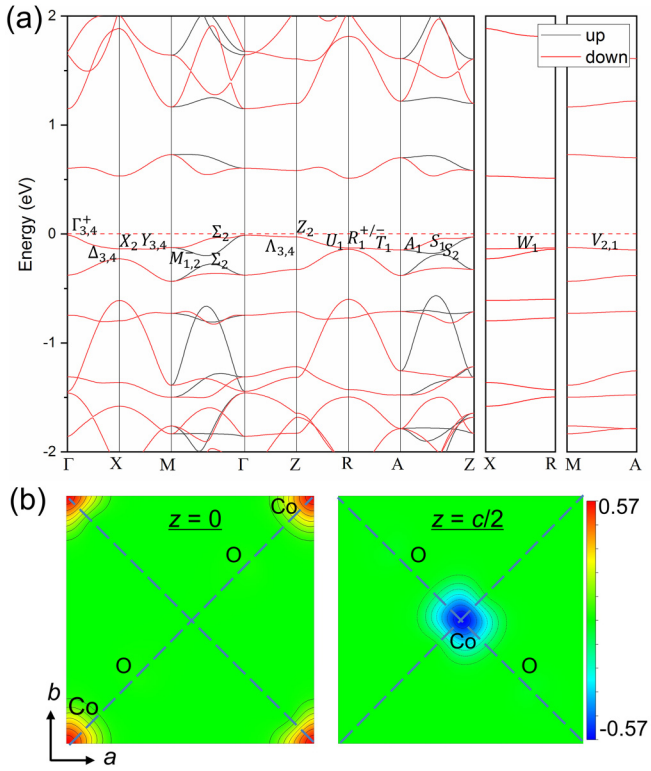

FIG. 4. (a) The calculated spin polarized band structure, without considering the on-site Coulomb interaction of Co atoms ($U = 0$ eV). The horizontal dashed line denotes the Fermi energy. The representation labels are the same as those in Ref. [75]. The representation of R can be either R_1^+ or R_1^-. (b) The magnetization density of CTO on the (001) plane at $z = 0$ and $c/2$, respectively, c is the lattice constant along z direction. The positions of Co and O atoms are indicated.

Our first-principles calculations reveal that, when the oxygen vacancy is located at the $4f$ sites, there is a net magnetic moment $\sim -1.8\,\mu_B$ in the supercell, corresponding to a saturation magnetization of $0.18\,\mu_B$ per Co atom. However, in the $8j$ oxygen vacancy case, there is no net magnetic moment in the supercell. Apparently, anions and vacancies are ordered in $CoTa_2O_{6-x}N_{2x/3}\square_{x/3}$ as reasonably restrained during the structural refinements in Fig. S6 (Supplemental Material [26]). We show the magnetization densities in the *ab* plane in Figs. 6(c) and 6(d) since the magnetic moments of Co atoms mainly interact and lie in this plane. From Fig. 6(c), it is clear that the magnetic moment of one Co atom with CoO_5N coordination ($Co_{3,a}$) is reduced in the $4f$ case. We further find that the magnetic moments of other two Co atoms ($Co_{8,a}$ and $Co_{8,b}$) with CoO_5N coordination remain the same as that of the bulk Co atom. This different behavior comes from the fact that, in $Co_{3,a}$, the Co-N bond is not located in the *ab* plane and about which the mirror symmetry is broken. The shape of the magnetization density of $Co_{6,a}$ with CoO_5 coordination changes a little but is still along [1–3,3–9] or [−110], and the magnitude of the magnetic moment is not changed. There is no visible change of the magnetization density of $Co_{3,b}$ with CoO_4N coordination, and the magnitude of the magnetic moment remains the same as those in the bulk. Physically, this behavior can be explained by inspecting the partial density of states (PDOS) of the d orbitals of the Co atom, which reflects the effect of the crystal field of nearby coordination (O_6, O_5N, O_4N, etc.), as exemplified in Fig. S13 (Supplemental Material [26]).

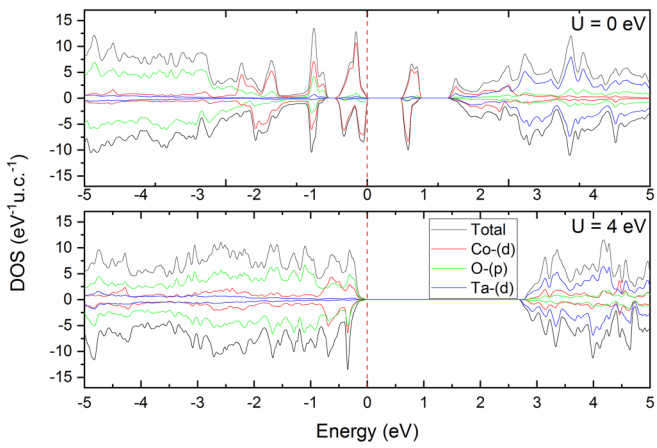

FIG. 5. The density of states near the Fermi energy of CTO, without (upper panel, $U = 0$ eV) and with (lower panel, $U = 4.0$ eV) onsite Coulomb interaction of Co atoms. The vertical dashed line denotes the Fermi energy.

We are now safe to arrive at the conclusion that the inclusion of nitrogen dopant in CTO, with Co-N bond not in the *ab* plane and coordination of Co atom with O_5N, can turn the sample from antiferromagnet to ferrimagnet, and the slight hysteretic loop $M(H)$ in Fig. 3 is a direct consequence of this transition. As shown in Figs. 6(e)–6(g), a ferrimagnet can be deconstructed into an antiferromagnet and a ferromagnet, and the magnetization curve under an external field can be decomposed into an AFM component M_{AFM} and a FM component M_{FM}. Note that, in the FM sublattice, the number of magnetic moments per unit volume n_{FM} is much smaller than the number of magnetic moments per unit volume in the AFM sublattice n_{AFM} and is dependent on the doping ratio x. Since there is no experimental evidence that the CoO_5N is ordered and considering the low density of "magnetic ion" CoO_5N, the ferrimagnet model adopted by calculation is not able to explain the high Curie temperature and ferromagnetism found here. However, the model indicates that there might be some mechanism like that in DMS, the only difference being that, in DMS, the host is a nonmagnetic semiconductor [80], but here, the host is an antiferromagnet. This DMS system with an AFM host deserves further study. Note that the saturation magnetization is proportional to the magnetic moments per unit volume; thus, the dilute magnetic ions should reach saturation at much lower external field than that of the AFM host. The discontinuity at 0.5 T in the magnetization curves is thus understood as the saturation field of the dilute magnetic ions part.

3. Predicted pressure effect on the electronic structure

Extrinsic pressure has proven to be powerful to tune the properties in 2D materials [15–17]. Here, we further analyze the behavior of the electronic structure of CTO under high pressure, assuming there is no structural phase transition, that

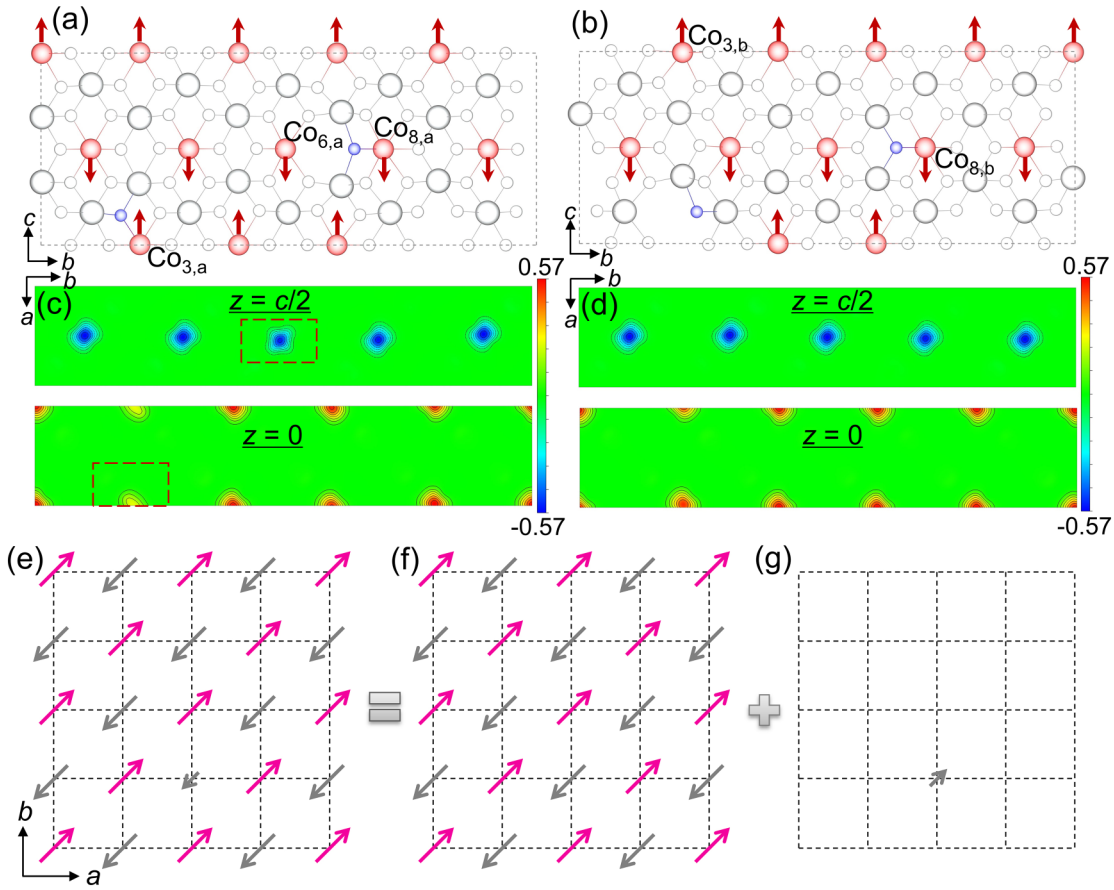

FIG. 6. The supercell with two nitrogen dopant and one oxygen vacancy, corresponding to $CoTa_2O_{6-x}N_{2x/3}\square_{x/3}$, $x = 0.3$. The oxygen vacancy can be located at (a) Wyckoff position $4f$ $(x, x, 0)$ or (b) $8j$ (x, x, z). The red, gray, white, and blue spheres represent cobalt, tantalum, oxygen, and nitrogen atoms, respectively. The arrows on cobalt atoms indicate the magnetic moments. The corresponding magnetization density on the (001) plane, with oxygen vacancy at (c) $4f$ and (d) $8j$, respectively. The $z = c/2$ case is in the upper panel and $z = 0$ case in the lower panel. Illustration of the fact that (e) a ferrimagnet can be decomposed into (f) an antiferromagnet and (g) a ferromagnet.

is, the space group $P4_2/mnm$ is maintained. Figure 7(a) shows the variation of total energy with respect to unit cell volume, which has an inflection point near $V = 190\,\text{Å}^3$, indicating the existence of an electronic phase transition. By fitting the data to the Murnaghan equation for $V < 190\,\text{Å}^3$ (phase 2) and $V > 190\,\text{Å}^3$ (phase 1), respectively, we obtained the pressure dependence of the relative enthalpies (ΔH, or Gibbs free energies at zero temperature) between the two phases (Fig. S14, Supplemental Material [26]). The phase transition occurs at pressure ~ 24.5 GPa. The variation of volume with pressure is shown in Fig. S15 (Supplemental Material [26]), from which the discontinuity of volume at the transition point is clearly seen, and the pressure at a certain volume can be determined. The phase transition is also manifested in the variation of lattice constants with respect to volume (or pressure), as shown in Fig. S16 (Supplemental Material [26]).

CTO becomes metallic in phase 2, as shown in Fig. S17 (Supplemental Material [26]), indicating that the phase transition is an insulator-to-metal transition. The most striking feature here is that, after entering the metallic state, the magnetic moment of Co disappears, and CTO becomes nonmagnetic. This is manifested by the drop to zero of the values of the magnetic moment of Co in Fig. 7(a) and the disappearance of the k-dependent splitting between spin-up and spin-down energy bands along ΓM and ZA. Here, we note that, before entering the nonmagnetic metallic phase, CTO is in a border phase with a low-spin state for Co^{2+}, as manifested by the four data points near $V = 190\,\text{Å}^3$ in the magnetic moment-volume curve in Fig. 7(a). This transition is due to the crystal field splitting between e_g and t_{2g} orbitals (actually e_g and t_{2g} are nondegenerate here due to the D_{2h} site symmetry of Co, but the deviation may not be large) becoming larger than the Coulomb interaction as pressure increases. Note that, for Co^{2+} with six-coordination, the radius for high-spin and low-spin states are 0.745 and 0.65 Å, respectively [38]. The radius of three-coordinated O^{2-} is 1.36 Å. We thus have bond length of the Co-O bond of 2.105 and 2.01 Å, respectively. The variation of the calculated Co-O bond lengths with respect to volume is shown in Fig. 7(b). The bond length of the Co-O bond with low-spin Co^{2+} state just locates at the position where CTO enters in the border phase. The reason why, as pressure increases (volume decreases), the magnetic moment of Co becomes zero is still not clear. However, the PDOS of Co in such a high-pressure condition shows that the PDOS of d_{x2-y2} orbital is zero, indicating that this orbital might not be occupied. Further experimental work is needed to explain this phenomenon. The behavior of the electronic structure of nitrogen-doped CTO under high pressure is out of

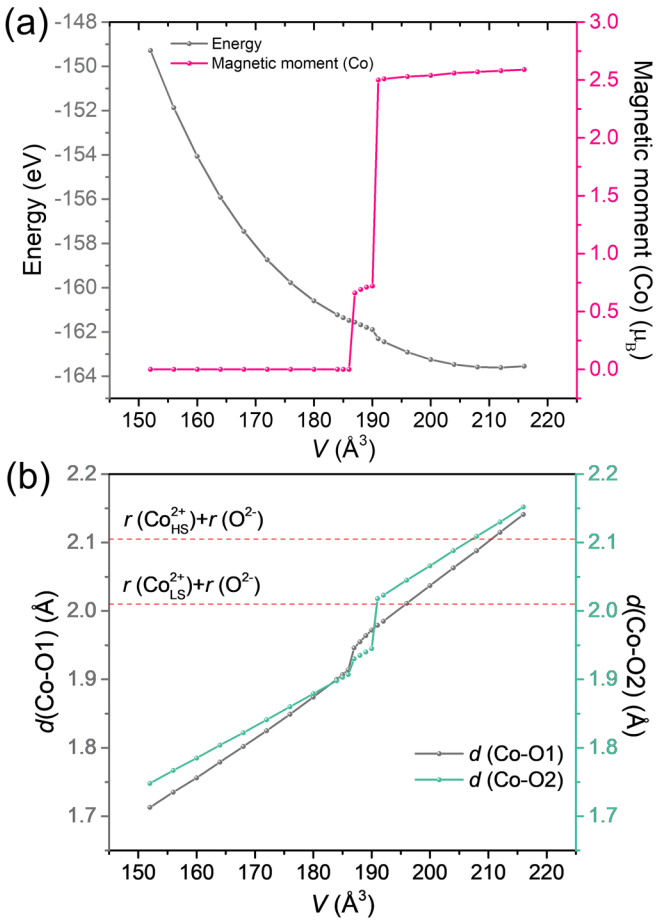

FIG. 7. (a) The variation of total energy and the average absolute value of magnetic moments of Co atoms in CTO with the unit cell volume. Near $V = 190$ Å^3 there is a clear inflection point in the E-V curve, associated with discontinuous change of magnetic moment of Co atom. (b) The evolution of the bond length of Co-O1 bond (in *ab* plane) and Co-O2 bond (not in *ab* plane) with unit cell volume. The sum of the radius of Co^{2+} with coordination six and O^{2-} with coordination three are shown, for high-spin and low-spin Co states, respectively.

the scope of this paper; it is anticipated that a similar insulator-to-metal transition can occur. However, due to the presence of nitrogen dopant and oxygen vacancy, the magnetic moment of Co surrounded by those vacancies may not vanish, and the sample would turn into a FM metal.

III. SUMMARY

In summary, we have successfully synthesized the anionic (O^{2-}/N^{3-}) and vacancy-ordered oxynitrides $CoTa_2O_{6-x}N_{2x/3}\square_{x/3}$ ($x = 0.015$, 0.05, and 0.15) via thermal ammonolysis of $CoTa_2O_6$, in which the nitrogen contents were adjusted by reaction temperature. The nitrided samples demonstrate narrowing band gaps, from 3.22 eV for $CoTa_2O_6$ to 3.02 eV for $CoTa_2O_{5.85}N_{0.1}\square_{0.15}$, and above-RT FM response. First-principles calculations reveal that the emerging ferromagnetism is engineered by the CoO_5N configuration caused by nitrogen doping, which evokes the transformation of octahedral configuration of cobalt and energy level, leading to change in magnetic moment. An insulator-to-metal transition is also predicted to arise ~24.5 GPa due to an electronic phase transition accompanied with the collapse of magnetic moments. These discoveries identified a simple and effective approach to realize practical ferromagnetism and are expected to forward a mechanism of magnetic transitions and advance exploration of 2D oxides for spintronic devices.

ACKNOWLEDGMENTS

This paper was supported by the National Science Foundation of China (Grants No. NSFC-22090041 and No. 21875287), the Program for Guangdong Introducing Innovative and Entrepreneurial Teams (2017ZT07C069). Y.Z. and D.X.Y. are supported by NKRDPC-2018YFA0306001, NKRDPC-2017YFA0206203, NSFC-11974432, GBABRF-2019A1515011337, Leading Talent Program of Guangdong Special Projects, and National Science Foundation (NSF-DMR-1507252). Work at Brookhaven National Laboratory was supported by the DOEBES (DE-SC0012704). The theoretical part in this paper was performed on TianHe-2 at the National Supercomputer Center in Guangzhou. The authors would like to thank Dr. Z. Deng at Institute of Physics, Chinese Academy of Sciences for helpful discussion of the magnetic measurements and K. Huang at School of Physical and Mathematical Sciences, Nanyang Technological University for valuable discussions.

[1] K. Ando, Science **312**, 1883 (2006).
[2] A. H. MacDonald, P. Schiffer, and N. Samarth, Nat. Mater. **4**, 195 (2005).
[3] P. Sharma, A. Gupta, K. V. Rao, F. J. Owens, R. Sharma, R. Ahuja, J. M. O. Guillen, B. Johansson, and G. A. Gehring, Nat. Mater. **2**, 673 (2003).
[4] B. Huang, G. Clark, E. Navarro-Moratalla, D. R. Klein, R. Cheng, K. L. Seyler, D. Zhong, E. Schmidgall, M. A. McGuire, D. H. Cobden, W. Yao, D. Xiao, P. Jarillo-Herrero, and X. Xu, Nature **546**, 270 (2017).
[5] P. van der Straten, Nature **498**, 175 (2013).
[6] W. Yan, Z. Sun, Z. Pan, Q. Liu, T. Yao, Z. Wu, C. Song, F. Zeng, Y. Xie, T. Hu, and S. Wei, Appl. Phys. Lett. **94**, 042508 (2009).
[7] D. Wang, Q. Chen, G. Xing, J. Yi, S. Rahman Bakaul, J. Ding, J. Wang, and T. Wu, Nano Lett. **12**, 3994 (2012).
[8] X. Liu, F. Lin, L. Sun, W. Cheng, X. Ma, and W. Shi, Appl. Phys. Lett. **88**, 062508 (2006).
[9] H. Liu, X. Zhang, L. Li, Y. X. Wang, K. H. Gao, Z. Q. Li, R. K. Zheng, S. P. Ringer, B. Zhang, and X. X. Zhang, Appl. Phys. Lett. **91**, 072511 (2007).
[10] Y. Liu, S. Feng, Z. Li, L. Zhang, G. Wang, W. Chen, T. Wang, and W. Zhong, RSC Adv. **6**, 57013 (2016).
[11] G. Yang, D. Gao, J. Zhang, J. Zhang, Z. Shi, and D. Xue, J. Phys. Chem. C **115**, 16814 (2011).
[12] C.-Q. Luo, S.-C. Zhu, C.-H. Lam, and F. C.-C. Ling, Mater. Res. Express **7**, 076103 (2020).

[13] M. Seike, K. Sato, and H. Katayama-Yoshida, Jpn. J. Appl. Phys. **50**, 090204 (2011).

[14] K. Kenmochi, M. Seike, K. Sato, A. Yanase, and H. Katayama-Yoshida, J. Appl. Phys. **43**, L934 (2004).

[15] T. Li, S. Jiang, N. Sivadas, Z. Wang, Y. Xu, D. Weber, J. E. Goldberger, K. Watanabe, T. Taniguchi, C. J. Fennie, K. Fai Mak, and J. Shan, Nat. Mater. **18**, 1303 (2019).

[16] T. Song, Z. Fei, M. Yankowitz, Z. Lin, Q. Jiang, K. Hwangbo, Q. Zhang, B. Sun, T. Taniguchi, K. Watanabe, M. A. McGuire, D. Graf, T. Cao, J.-H. Chu, D. H. Cobden, C. R. Dean, D. Xiao, and X. Xu, Nat. Mater. **18**, 1298 (2019).

[17] J.-H. Yang and H. Xiang, Nat. Mater. **18**, 1273 (2019).

[18] A. P. Nayak, Z. Yuan, B. Cao, J. Liu, J. Wu, S. T. Moran, T. Li, D. Akinwande, C. Jin, and J. F. Lin, ACS Nano **9**, 9117 (2015).

[19] A. P. Nayak, S. Bhattacharyya, J. Zhu, J. Liu, X. Wu, T. Pandey, C. Jin, A. K. Singh, D. Akinwande, and J. F. Lin, Nat. Commun. **5**, 3731 (2014).

[20] T. A. Tartaglia, J. N. Tang, J. L. Lado, F. Bahrami, M. Abramchuk, G. T. McCandless, M. C. Doyle, K. S. Burch, Y. Ran, J. Y. Chan, and F. Tafti, Sci. Adv. **6**, eabb9379 (2020).

[21] L. Cai, J. He, Q. Liu, T. Yao, L. Chen, W. Yan, F. Hu, Y. Jiang, Y. Zhao, T. Hu, Z. Sun, and S. Wei, J. Am. Chem. Soc. **137**, 2622 (2015).

[22] Y. Wen, Z. Liu, Y. Zhang, C. Xia, B. Zhai, X. Zhang, G. Zhai, C. Shen, P. He, R. Cheng, L. Yin, Y. Yao, M. Getaye Sendeku, Z. Wang, X. Ye, C. Liu, C. Jiang, C. Shan, Y. Long, and J. He, Nano Lett. **20**, 3130 (2020).

[23] D. Zhong, K. L. Seyler, X. Linpeng, R. Cheng, N. Sivadas, B. Huang, E. Schmidgall, T. Taniguchi, K. Watanabe, M. A. McGuire, W. Yao, D. Xiao, K.-M. C. Fu, and X. Xu, Sci. Adv. **3**, e1603113 (2017).

[24] S. A. Chambers, T. C. Droubay, C. M. Wang, K. M. Rosso, S. M. Heald, D. A. Schwartz, K. R. Kittilstved, and D. R. Gamelin, Mater. Today **9**, 28 (2006).

[25] E. J. Kinast, C. A. dos Santos, D. Schmitt, O. Isnard, M. A. Gusmão, and J. B. M. da Cunha, J. Alloys Compd. **491**, 41 (2010).

[26] See Supplemental Material at http://link.aps.org/supplemental/10.1103/PhysRevB.104.014421 for details of the experiments, chemical and spectroscopic characterization, optical and magnetic properties, theoretical simulation of the relationship between pressure and the relative enthalpies or unit cell volume of CTO and the spin polarized band structure of CTO, and including Refs. [25,33–37,42–64,69–72,77].

[27] T. Oshima *et al.*, Angew. Chem. Int. Ed. **57**, 8154 (2018).

[28] M. Ohashi, K. Kusumoto, T. Sugiyama, and K. Kato, J. Ceram. Soc. Jpn. **126**, 66 (2018).

[29] A. Maegli, S. Yoon, E. Otal, L. Karvonen, P. Mandaliev, and A. Weidenkaff, J. Solid State Chem. **184**, 929 (2011).

[30] K. Hibino, M. Yashima, T. Oshima, K. Fujii, and K. Maeda, Dalton Trans. **46**, 14947 (2017).

[31] R. Marchand, Y. Laurent, J. Guyader, P. L'Haridon, and P. Verdier, J. Eur. Ceram. Soc. **8**, 197 (1991).

[32] A. Rachel, S. G. Ebbinghaus, M. Güngerich, P. J. Klar, J. Hanss, A. Weidenkaff, and A. Reller, Thermochim. Acta **438**, 134 (2005).

[33] C. de la Calle, J. Sánchez-Benítez, F. Barbanson, N. Nemes, M. T. Fernández-Díaz, and J. A. Alonso, J. Appl. Phys. **109**, 123914 (2011).

[34] M. Lv, X. Sun, S. Wei, C. Shen, Y. Mi, and X. Xu, ACS Nano **11**, 11441 (2017).

[35] A. A. Coelho, *Topas V6: General Profile and Structure Analysis Software for Powder Diffraction Data—User's Manual* (Bruker AXS, Karlsruhe, 2017).

[36] A. B. Christian, A. T. Schye, K. O. White, and J. J. Neumeier, J. Phys. Condens. Matter **30**, 195803 (2018).

[37] F. Liu, B. Wang, X. Yang, Y. Guan, Q. Wang, X. Liang, P. Sun, Y. Wang, and G. Lu, Sens. Actuators B Chem. **240**, 148 (2017).

[38] R. D. Shannon, Acta Cryst. **A32**, 751 (1976).

[39] P. Antoine, R. Assabaa, P. L'Haridon, R. Marchand, and Y. Laurent, Mater. Sci. Eng. **B5**, 43 (1989).

[40] A. Fuertes, J. Mater. Chem. **22**, 3293 (2012).

[41] M. Kitano, J. Kujirai, K. Ogasawara, S. Matsuishi, T. Tada, H. Abe, Y. Niwa, and H. Hosono, J. Am. Chem. Soc. **141**, 20344 (2019).

[42] Z. Deng, M. Retuerto, S. Liu, M. Croft, P. W. Stephens, S. Calder, W. Li, B. Chen, C. Jin, Z. Hu, M.-R. Li, H.-J. Lin, T.-S. Chan, C.-T. Chen, S. W. Kim, and M. Greenblatt, Chem. Mater. **30**, 7047 (2018).

[43] C. E. Frank, E. E. McCabe, F. Orlandi, P. Manuel, X. Tan, Z. Deng, M. Croft, V. Cascos, T. Emge, H. L. Feng, S. Lapidus, C. Jin, M. Wu, M. R. Li, S. Ehrlich, S. Khalid, N. Quackenbush, S. Yu, D. Walker, and M. Greenblatt, Chem. Commun. **55**, 3331 (2019).

[44] J. E. Sunstrom, K. V. Ramanujachary, M. Greenblatt, and M. Croft, J. Solid State Chem. **139**, 388 (1998).

[45] T. K. Mandal, M. Croft, J. Hadermann, G. Van Tendeloo, P. W. Stephens, and M. Greenblatt, J. Mater. Chem. **19**, 4382 (2009).

[46] M. R. Li, D. Walker, M. Retuerto, T. Sarkar, J. Hadermann, P. W. Stephens, M. Croft, A. Ignatov, C. P. Grams, J. Hemberger, I. Nowik, P. S. Halasyamani, T. T. Tran, S. Mukherjee, T. S. Dasgupta, and M. Greenblatt, Angew. Chem. Int. Ed. **52**, 8406 (2013).

[47] C. A. Marjerrison, C. M. Thompson, A. Z. Sharma, A. M. Hallas, M. N. Wilson, T. J. S. Munsie, R. Flacau, C. R. Wiebe, B. D. Gaulin, G. M. Luke, and J. E. Greedan, Phys. Rev. B **94**, 134429 (2016).

[48] G. Popov, M. Greenblatt, and M. Croft, Phys. Rev. B **67**, 024406 (2003).

[49] B. J. Kim, H. Jin, S. J. Moon, J. Y. Kim, B. G. Park, C. S. Leem, J. Yu, T. W. Noh, C. Kim, S. J. Oh, J. H. Park, V. Durairaj, G. Cao, and E. Rotenberg, Phys. Rev. Lett. **101**, 076402 (2008).

[50] H. L. Feng, Z. Deng, C. U. Segre, M. Croft, S. H. Lapidus, C. E. Frank, Y. Shi, C. Jin, D. Walker, and M. Greenblatt, Inorg. Chem. **60**, 1241 (2020).

[51] C. Martins, M. Aichhorn, and S. Biermann, J. Phys. Condens. Matter **29**, 263001 (2017).

[52] R. Zhang, Y. Lu, L. Wei, Z. Fang, C. Lu, Y. Ni, Z. Xu, S. Tao, and P. Li, J. Mater. Sci. Mater. Electron. **26**, 9941 (2015).

[53] G. Huang, Z. Xiao, R. Chen, and S. Wang, ACS Sustain. Chem. Eng. **6**, 15954 (2018).

[54] Z. Hua, X. Zhang, X. Bai, L. Lv, Z. Ye, and X. Huang, J. Colloid Interface Sci. **450**, 45 (2015).

[55] M. Higashi, K. Domen, and R. Abe, Energy Environ. Sci. **4**, 4138 (2011).

[56] E. S. Kim, N. Nishimura, G. Magesh, J. Y. Kim, J. W. Jang, H. Jun, J. Kubota, K. Domen, and J. S. Lee, J. Am. Chem. Soc. **135**, 5375 (2013).

[57] Q. Gao, S. Wang, Y. Ma, Y. Tang, C. Giordano, and M. Antonietti, Angew. Chem. Int. Ed. **51**, 961 (2012).
[58] P. Arunachalam, M. Shaddad, M. Ghanem, A. Al-Mayouf, and M. Weller, Nanomaterials **8**, 48 (2018).
[59] B. Cao, G. M. Veith, R. E. Diaz, J. Liu, E. A. Stach, R. R. Adzic, and P. G. Khalifah, Angew. Chem. Int. Ed. **52**, 10753 (2013).
[60] X. Zhang, J. Hu, Y. Cao, J. Xie, W. Jia, S. Wang, and D. Jia, Chem. Eur. J. **24**, 14111 (2018).
[61] H. Jiang, W. Zhang, S. Zang, and W. Zhang, Int. J. Hydrog. Energy **44**, 24218 (2019).
[62] E. Nurlaela, M. Harb, S. del Gobbo, M. Vashishta, and K. Takanabe, J. Solid State Chem. **229**, 219 (2015).
[63] S. Bhattacharyya, S. Kurian, S. M. Shivaprasad, and N. S. Gajbhiye, J. Nanopart. Res. **12**, 1107 (2009).
[64] M. Jae Kwon, H. Jung, and J. Hoon Park, J. Phys. Chem. Solids **73**, 1448 (2012).
[65] M. Takano and T. Takada, Mater. Res. Bull. **5**, 449 (1970).
[66] X. Yin, Y. Wang, R. Jacobs, Y. Shi, I. Szlufarska, D. Morgan, and X. Wang, Nano Lett. **19**, 7085 (2019).
[67] W. Yu, J. Li, T. S. Herng, Z. Wang, X. Zhao, X. Chi, W. Fu, I. Abdelwahab, J. Zhou, J. Dan, Z. Chen, Z. Chen, Z. Li, J. Lu, S. J. Pennycook, Y. P. Feng, J. Ding, and K. P. Loh, Adv. Mater. **31**, 1903779 (2019).
[68] J. N. Reimers, J. E. Greedan, C. V. Stager, and R. Kremer, J. Solid State Chem. **83**, 20 (1989).
[69] G. Kresse and D. Joubert, Phys. Rev. B **59**, 1758 (1999).
[70] J. P. Perdew, K. Burke, and M. Ernzerhof, Phys. Rev. Lett. **77**, 3865 (1996).
[71] P. E. Blochl, Phys. Rev. B **50**, 17953 (1994).
[72] H. J. Monkhorst and J. D. Pack, Phys. Rev. B **13**, 5188 (1976).
[73] L. D. Yuan, Z. Wang, J. W. Luo, E. I. Rashba, and A. Zunger, Phys. Rev. B **102**, 014422 (2020).
[74] J. Coey, *Magnetism and Magnetic Materials* (Cambridge University Press, Cambridge, 2010), Chap. 4.
[75] J. O. Dimmock and R. G. Wheeler, Phys. Rev. **127**, 391 (1962).
[76] A. V. Shubnikov and W. T. Holser, *Colored Symmetry* (Pergamon, London, 1964).
[77] S. L. Dudarev, G. A. Botton, S. Y. Savrasov, C. J. Humphreys, and A. P. Sutton, Phys. Rev. B **57**, 1505 (1998).
[78] P. Hohenberg and W. Kohn, Phys. Rev. **136**, B864 (1964).
[79] W. Kohn and L. J. Sham, Phys. Rev. **140**, A1133 (1965).
[80] H. Saito, V. Zayets, S. Yamagata, and K. Ando, Phys. Rev. Lett. **90**, 207202 (2003).